Resolution doubling in fluorescence microscopy with confocal spinning-disk image scanning microscopy

Olaf Schulz[a,b], Christoph Pieper[a,b], Michaela Clever[c], Janine Pfaff[d], Aike Ruhlandt[e], Ralph H. Kehlenbach[d], Fred S. Wouters[b,f], Jörg Großhans[c], Gertrude Bunt[b,f], and Jörg Enderlein[a,b,1]

[a]Third Institute of Physics–Biophysics and [e]Institute for X-Ray Physics, Georg-August University, 37077 Göttingen, Germany; [b]Deutsche Forschungsgemeinschaft Research Center "Nanoscale Microscopy and Molecular Physiology of the Brain," Göttingen, Germany; [c]Institute of Biochemistry and Molecular Cell Biology, Department of Developmental Biochemistry, Göttingen University Medical School, 37077 Göttingen, Germany; [d]Department of Molecular Biology, Medical Faculty, Georg-August University, 37073 Göttingen, Germany; and [f]Molecular and Cellular Systems, Institute for Neuro- and Sensory Physiology, University Medicine Göttingen, 37073 Göttingen, Germany

Edited* by W. E. Moerner, Stanford University, Stanford, CA, and approved November 13, 2013 (received for review August 22, 2013)

We demonstrate how a conventional confocal spinning-disk (CSD) microscope can be converted into a doubly resolving image scanning microscopy (ISM) system without changing any part of its optical or mechanical elements. Making use of the intrinsic properties of a CSD microscope, we illuminate stroboscopically, generating an array of excitation foci that are moved across the sample by varying the phase between stroboscopic excitation and rotation of the spinning disk. ISM then generates an image with nearly doubled resolution. Using conventional fluorophores, we have imaged single nuclear pore complexes in the nuclear membrane and aggregates of GFP-conjugated Tau protein in three dimensions. Multicolor ISM was shown on cytoskeletal-associated structural proteins and on 3D four-color images including MitoTracker and Hoechst staining. The simple adaptation of conventional CSD equipment allows superresolution investigations of a broad variety of cell biological questions.

Fluorescence microscopy is an extremely powerful research tool in the life sciences. It combines highest sensitivity with molecular specificity and exceptional image contrast. However, as with all light-based microscopy techniques, its resolution is limited by the diffraction of light to a typical lateral resolution of ∼200 nm and an axial resolution of ∼500 nm (for 500-nm wavelength light). Only recently, this diffraction limit was broken by using the quantum, or nonlinear, character of fluorescence excitation and emission. The first of these superresolution methods was stimulated emission depletion (STED) microscopy (1). Later, methods based on single-molecule localization, such as photoactivated localization microscopy (PALM) (2) and stochastic optical reconstruction microscopy (STORM) (3), joined the field. These methods "break" the diffraction limit because they all use principles that operate beyond the diffraction of light.

Although still bound to light diffraction, increased spatial resolution can be achieved in a class of advanced resolution methods that exploit a clever combination of excitation and detection modalities (4–7). Although these methods do not reach the resolution achievable with STED, PALM, STORM, and related techniques, they do not require any specialized labels or high excitation intensities, and they may be applied to any fluorescent sample at any excitation/emission wavelength. The most prominent example of this class is structured illumination microscopy (SIM) (5), in which one scans a sample with a structured illumination pattern while taking images with a wide-field imaging system. Meanwhile, several commercial instruments for SIM have become available. The disadvantages of SIM are its technical complexity, reflected in the rather large cost of the commercially available systems, and its sensitivity to optical imperfections and aberrations, which are unavoidable in biological samples.

In a theoretical study in 1988, Sheppard (8) pointed out that it is possible to double the resolution of a scanning confocal microscope in a manner closely related to SIM. In SIM, one starts with a conventional wide-field imaging microscope, and by implementing a scanning structured illumination, one subsequently obtains, after appropriate deconvolution of the recorded images, an image with increased resolution. In image-scanning microscopy (ISM), as proposed by Sheppard, one starts with a conventional confocal microscope that uses a diffraction-limited laser focus for scanning a sample but replaces the point detector typically used for recording the excited fluorescence signal with an imaging detector. Also here, an image with enhanced resolution is obtained after applying an appropriate algorithm to the recorded images.

We experimentally realized this idea first in 2010 (4), indeed demonstrating a substantial increase in resolution. The major drawback of this implementation was the slowness of the imaging. At each scan position of the laser focus, an image of the excited region had to be recorded, limiting the scan speed by the frame rate of the imaging camera used. For the small scan area of 2 μm × 2 μm shown with the original ISM setup, data acquisition took 25 s. In 2012, York et al. (6) demonstrated that this limitation may be overcome by using a multifocal excitation scheme. They generated an array of multiple excitation foci by implementing a digital micro-mirror device (DMD) into the excitation path of a wide-field microscope. Using this system, ISM images can be obtained with excellent speed, in two excitation/emission wavelengths (two-color imaging) and in three dimensions. However, this approach requires the incorporation of a DMD with all the necessity of perfect optical alignment.

Here, we demonstrate that existing imaging detector-based confocal systems can be converted easily into a doubly resolving ISM system. This mainly includes two kinds of microscopes that are widely available in research laboratories: confocal spinning-disk

Significance

Fluorescence microscopy is an enormously powerful tool for investigating structural organization and dynamical processes on the cellular level because of its noninvasiveness, sensitivity, and specificity. However, classical fluorescence microscopy is limited in resolution by the diffraction of light. In recent years, structural illumination microscopy has succeeded in doubling this resolution without requiring any special sample preparation or labeling dyes. However, it is technically very challenging and complex. Here, we present an alternative that achieves the same resolution enhancement by using a standard confocal spinning-disk microscope with minimal modifications. This method, in principle, allows one to double the resolution of any existing confocal microscope.

Author contributions: R.H.K., F.S.W., J.G., G.B., and J.E. designed research; O.S., C.P., M.C., J.P., F.S.W., and G.B. performed research; O.S., C.P., A.R., and J.E. contributed new reagents/analytic tools; O.S. and M.C. analyzed data; and O.S. and J.E. wrote the paper.

The authors declare no conflict of interest.

*This Direct Submission article had a prearranged editor.

[1]To whom correspondence should be addressed. E-mail: J.Enderlein@physik3.gwdg.de.

This article contains supporting information online at www.pnas.org/lookup/suppl/doi:10.1073/pnas.1315858110/-/DCSupplemental.

(CSD) microscopes and rapid laser scanning confocal microscopes with an imaging camera as the detector. We present the results obtained with a CSD system.

Results

CSD-Based Implementation of ISM. In ISM, the sample is excited by a tightly focused laser spot and the fluorescence light emerging from the focus is imaged by means of a camera. If the pixels of the camera are small enough, they may be considered "infinitely small pinholes" for the purpose of enhancing the lateral resolution. The beauty of CSD-based ISM (CSD-ISM) as a 3D super-resolution technique lies in the simplicity of the optical setup. The principle behind the use of CSD microscopy for ISM is based on the use of a camera and the inherent presence of many excitation foci that rapidly scan the sample. Here we show how the CSD can be upgraded easily to be used for ISM. Although it has been known for a while that a very small pinhole enhances the resolution in confocal microscopy (9), this approach is not practical, because almost all the fluorescent light is rejected by the pinhole. In the case of a camera, however, in which there are many pixels, we do not lose light because every (detectable) photon from the sample will be recorded on the camera chip. In this fashion, every pixel records a "perfect" confocal image. To obtain a final image that contains all the light from every pixel, the confocal images gathered by every pixel must be combined. For this, we need to consider the offset from the optical axis of each pixel and its effect on the image that this pixel records. If a pixel is shifted by a distance d from the optical axis, the image this pixel records will be shifted by $d/2$ with respect to an image recorded on the optical axis (*Theory of Image-Scanning Microscopy*). Fig. 1*B* explains graphically the origin of this factor 1/2. Thus, the fluorescence intensity information from each pixel must be shifted half its distance toward the optical axis, and summed to obtain the final image. Alternatively, and equivalently, the unmodified raw data can be registered in an image in which the scan coordinates are multiplied by two. This approach naturally leads to twice as many pixels in each dimension. For detailed information about the basics of ISM and the image calculation, please see *Theory of Image Scanning Microscopy* and *Fourier Reweighting* and Figs. S1 and S2.

To be able to apply the ISM method to data gathered with a CSD, one has to make sure the camera captures the light from individual pinholes without being smeared out while the disk spins. In our setup, this is achieved by means of stroboscopic illumination. The illuminating laser is active for only a few microseconds at a time; in this time, the disk has not rotated noticeably. The lasers and the camera are synchronized with the motion of the spinning disk. The synchronization, which is realized using programmable electronics [field-programmable gate array (FPGA)], allows an image to be recorded at a highly reproducible position of the disk during its motion. The whole image is "scanned" by introducing a delay to the laser trigger, which moves the illuminated spots through the sample. The positions of the spots are prerecorded for each time point by imaging a homogenously fluorescing sample. Details on the synchronization and calibration of the system may be found in *Methods* and in *ISM Algorithm and Image Calculation Using Matlab*.

The raw data collected by the CSD in ISM mode consists of a set of about 250 images. The sum of these images is equivalent to a regular CSD image. One CSD-ISM image can be acquired within 0.3–1 s, depending on the speed of the spin disk (1,500–5,000 rpm). For weakly fluorescing samples or to accommodate for a slower camera readout for larger fields of view, the camera can be read out only once while multiple laser triggers with the same delay are produced during multiple spin disk cycles. In this fashion, the signal-to-noise ratio is enhanced (*ISM Algorithm and Image Calculation Using Matlab*; Fig. S3). When presenting the experimental data below, we give the degree of averaging by noting the exposure time per frame, which is the laser pulse length times the number of cycles over which the image is accumulated, and the number of frames from which one ISM image is calculated. For a better comparison of all data, the total acquisition time of one ISM image also is given.

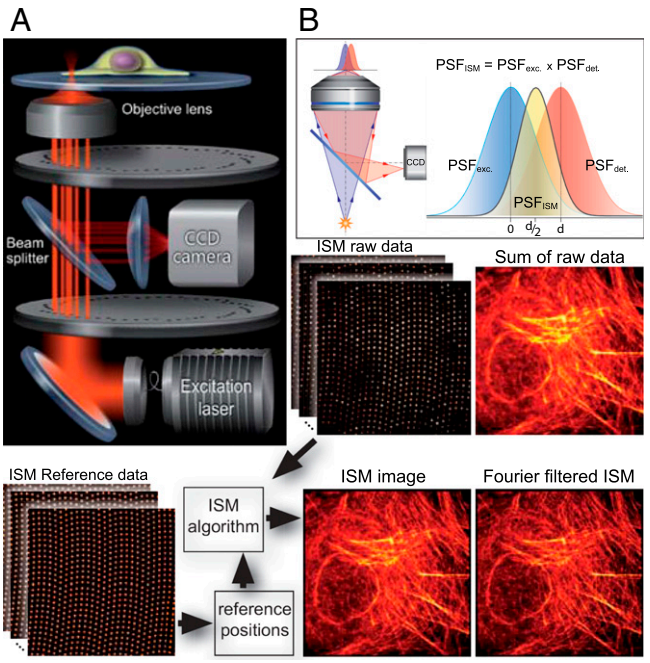

Fig. 1. Basics of CSD-ISM. (*A*) Schematic drawing of the optical setup. The excitation light (400 nm, 488 nm, 561 nm, or 647 nm) is coupled into the spin-disk confocal unit via an optical fiber. A Nipkow disk with microlenses focuses the light onto pinholes of an opposing disk. The microscope objective focuses the light emerging from the pinholes to diffraction-limited spots in the sample. The fluorescence emission from these spots is collected by the same objective and passes through the pinholes onto a CCD camera via a dichroic beam splitter. (*B*) A pixel on the CCD camera, if it is small enough, detects light from a diffraction-limited region of the sample. Pixels offset from the optical axis will detect an area of the sample that does not coincide with the excitation; thus, the product of these two point-spread functions, which is proportional to the amount of light detected, will be shifted. This way, each pixel on the CCD records a confocal image that is shifted by half its distance from the optical axis. The bottom of the figure illustrates the work flow in CSD-ISM. Reference data from a homogenously fluorescing sample is recorded to determine the center position of each pinhole. These reference positions are fed into the ISM algorithm that shifts the raw data from every pinhole, as indicated in *B*. Finally, Fourier filtering is performed to gain the full resolution enhancement of ISM.

We applied the ISM algorithm to each focal spot in each image, as indicated in Fig. 1. After applying the ISM algorithm to the raw data, the resolution can be enhanced further by Fourier reweighting, as described in ref. 4 (compare Figs. 1 and 2*C*, and *Fourier Reweighting*).

From the point of view of the optical setup, no modifications must be made for using a CSD for ISM. However, because the size of a pixel of the camera is a determining factor for the achievable resolution enhancement in ISM, the choice of camera and the magnification must be considered. In our case, we used a 100× objective and a camera adapter with 1.2× magnification. For our 16-μm pixel EM CCD, this translates to about a 133-nm effective pixel size. To obtain optimal ISM resolution (9), we added an additional 2× magnification to achieve a 67-nm pixel size. We also used a scientific complementary metal–oxide–semiconductor (sCMOS) camera with 6.5-μm pixels, which translates to about a 54-nm effective pixel size without additional magnification.

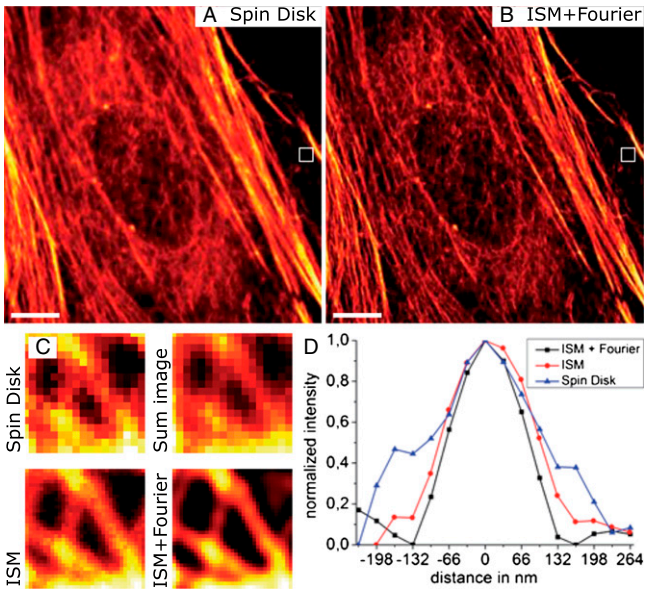

Fig. 2. Doubling the resolution for actin imaging in mammalian cells with CSD-ISM. Rat embryonal fibroblasts (REF52) were labeled for actin with Alexa 488–phalloidin. The exposure time for the conventional spin-disk image (*A*) was 10 ms. The CSD-ISM image (*B*) was calculated from 250 single images with an exposure time of 138 μs per frame (~20 s acquisition time). (*C*) Comparison of a small area (white frame) where individual actin filaments can be distinguished. The size of the magnified region is 1 μm. As expected, the conventional spin-disk image and the sum over all 250 single shots of the CSD-ISM dataset are of comparable quality, whereas the CSD-ISM image and the CSD-ISM image after Fourier reweighting show more detail. (*D*) The graphs show a section through the actin filament in the center of the zoom-in. Gaussian fits to these sections exhibit FWHMs of 201 nm, 162 nm, and 130 nm for the spin-disk image, the CSD-ISM image, and the Fourier reweighted CSD-ISM image, respectively. The scale bars in *A* and *B* are 5 μm.

Resolution in CSD-ISM. The resolution in ISM was estimated theoretically to be twice that of conventional wide-field microscopy (4). Experimentally, resolution enhancement factors of 1.63 (4) and 2 (6) were determined by measuring the apparent width of fluorescent beads (4, 6) and microtubules (6). To evaluate the resolution enhancement of our CSD-based ISM, we used single fluorescent molecules (Atto 655) and actin filaments labeled with Alexa 488 in a cell. Fig. 2*A* shows a regular CSD image of the actin network. The corresponding CSD-ISM image (Fig. 2*B*) clearly reveals a finer structure. The apparent width of the filaments was evaluated by zooming in on a region where individual actin filaments can be distinguished. Whereas the regular CSD image and the sum image of the ISM raw data are qualitatively similar, the CSD-ISM image and the Fourier reweighted CSD-ISM image clearly show more distinct structures (Fig. 2*C*). A section through the central filament in the indicated magnified region was used to estimate the enhanced resolution of CSD-ISM (Fig. 2*D*). For the CSD image, the FWHM, determined by a Gaussian fit, is 201 ± 20 nm (SE). From the CSD-ISM image, we measure an FWHM of 162 ± 10 nm, and 130 ± 10 nm for the Fourier reweighted CSD-ISM image, which translates to a resolution enhancement factor of 1.55. The theoretical values for the FWHMs of the point-spread functions of confocal and Fourier reweighted ISM (*Fourier Reweighting*) are 201 nm and 129 nm, respectively. These values were calculated assuming excitation at 488 nm and detection at 525 nm.

For a more rigorous evaluation of the resolution enhancement, we chose single molecules because they may be considered ideal point sources of fluorescence light. Because the brightness of the single molecules is too weak for high-speed imaging, averaging over longer exposure times was necessary. We imaged individual molecules of Atto 655, a fluorescence label shown to be very stable and to exhibit little blinking on glass surfaces under dry conditions (10). Two-dimensional Gaussians were fit to the single-molecule emission spots in the CSD image and in the CSD-ISM image for multiple scans. An example of the evolution from the CSD image, over the CSD-ISM image, to the final Fourier reweighted CSD-ISM image of a single Atto 655 molecule is given in Fig. 3*A*. The distribution of resolution values was determined from 86 molecules (histogram in Fig. 3*B*). For the CSD image, the mean of the distribution of FWHMs is 265 ± 27 nm (SD), and 197 ± 17 nm (SD) for the final CSD-ISM image. This corresponds to a resolution enhancement factor of 1.35. These values compare with theoretical values of 246 nm for confocal and 172 nm for Fourier reweighted ISM. The calculations were performed assuming excitation at 647 nm and detection at 690 nm.

The difference in the resolutions determined with the two test samples stems from their different excitation and emission wavelengths as the resolution of confocal microscopy, and thus ISM still depends on the wavelength of the light used.

In our present implementation of ISM, we use a simple but well-defined Fourier-reweighting procedure that enhances higher vs. lower frequencies in Fourier space for approaching the ideal optical transfer function of a microscope system with doubled resolution (4). More sophisticated algorithms, such as the popular Richardson–Lucy deconvolution (11–13), may give better results by better handling the inherent noisiness of real data but are not as straightforward and transparent as the Fourier-reweighting procedure used here.

ISM does not significantly enhance the axial resolution of a confocal microscope with a well-sized pinhole (*Theory of Image-Scanning Microscopy*), which also is what we observe in our data recorded with the CSD microscope.

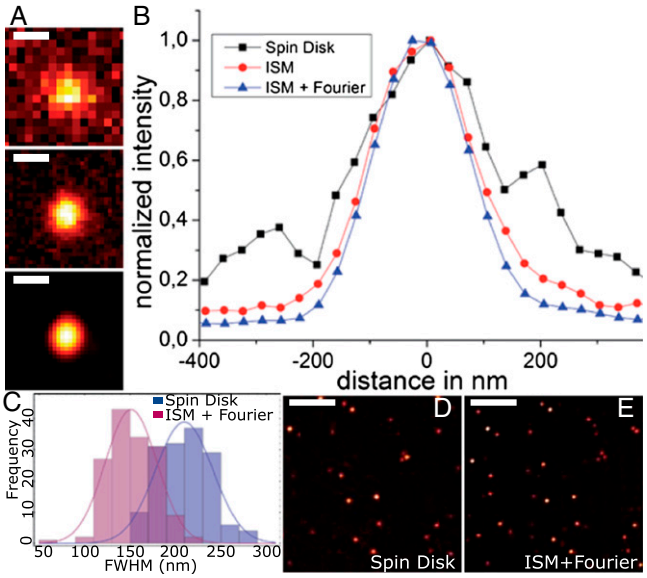

Fig. 3. Quantification of resolution enhancement using single Atto 655 molecules on glass. (*A*) Comparison among conventional spin disk, CSD-ISM, and CSD-ISM with Fourier reweighting of a single Atto 655 molecule. The spin-disk image (*D*) was taken at an exposure time of 1 s. The CSD-ISM image (*E*) was calculated from 1,000 single images, each with an exposure time of 138 μs (~80 s acquisition time). (*B*) Plot of a section through the center of the molecule for the different images in *A*. The FWHMs (Gauss fit) of the sections are 248 ± 12 nm, 186 ± 3 nm, and 171 ± 2 nm (SE), respectively. The histogram of FWHMs of single-molecule fluorescence (*C*) is determined by a 2D Gauss fit. The histogram contains both the *x* and *y* values of the FWHM of 86 single-molecule spots. The scale bar is 300 nm in *A* and 4 μm in *D* and *E*.

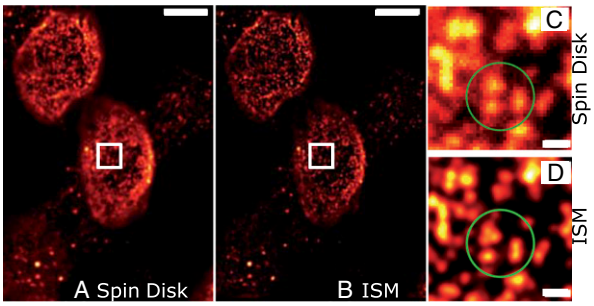

Fig. 4. Improved identification of single NPCs with CSD-ISM. Image of NPCs immunolabeled by mAb414 and Alexa 488. (*A*) Conventional spinning-disk image with an exposure time of 50 ms. (*B*) Final CSD-ISM image, calculated from 500 single images with an exposure of 138 μs per image (~40 s acquisition time). (*C* and *D*) Direct comparison of a smaller area between conventional spin disk (*C*) and CSD-ISM (*D*). The superior performance of CSD-ISM is immediately clear. Single NPCs, which were obscured in the confocal image, can be distinguished clearly (green circled area). The scale bars are 5 μm in the overview and 500 nm in the indicated magnified region.

Imaging of the Nuclear Pore Complex on the Nuclear Membrane. The nuclear pore complex (NPC) is an aqueous channel in the nuclear envelope that has a central role in the selective nuclear transport between cyto- and nucleoplasm. Accumulating evidence shows that the NPC has various regulatory functions, e.g., during development and aging (14–17). The structure of the metazoan NPC has been studied intensively by (cryo)electron microscopy, which revealed the hourglass-like shape whose diameter ranges from ~95 nm at the widest point to ~50 nm at the narrowest point, at the center of the NPC (18, 19). The eightfold arrangement of the NPC, which consists of multimeric subunits of more than 30 nucleoporins, was demonstrated recently by superresolution imaging by direct STORM (20). With a size close to the resolution of ISM at 488-nm excitation, single NPCs can be distinguished more clearly and accurately than from spin-disk images (Fig. 4). The NPC number and its distribution on the nuclear envelope change during the cell cycle (21); therefore, precise quantification is crucial. Whereas the measured NPC density from spin-disk images is only about 5.34 ± 0.28 NPC/μm^2, quantifications from CSD-ISM images yielded in an ~1.3-fold higher NPC density (7.01 ± 0.75 NPC/μm^2), which agrees very well with previously reported NPC densities in HeLa cells (21), confirming a relevant information gain with the superior CSD-ISM method.

Multicolor Imaging of the Cellular Cytoskeleton. Multicolor fluorescence imaging allows one to distinguish proteins and structures of interest and to study their colocalization and interactions. CSD-ISM is readily extendible to the imaging of multiple spectrally separable fluorescent labels. If no pulsed lasers are available in the existing CSD setup, the stroboscopic illumination of the sample can be achieved straightforwardly using an acousto-optical tunable filter (AOTF). In our setup, we used pulsed diode lasers at 400 nm, 488 nm, and 647 nm, and a 561-nm continuous wave (cw) laser with AOTF modulation. The different emission wavelengths may be imaged in sequential order, or beam splitters may be used to image different colors onto separate areas on the camera chip or onto separate cameras. Another way to realize simultaneous multicolor imaging is to modulate the lasers in quick succession so that their corresponding emission is separated properly on the camera (*Synchronization and Data Acquisition*).

To show the multicolor imaging potential of CSD-ISM, we labeled different cytoskeletal structures in rat embryonal fibroblasts (REF52). Actin was labeled with phalloidin–Alexa 488 tubulin by immunolabeling with TRITC, and the focal adhesion protein zyxin was labeled with Alexa 647. Comparison with the respective confocal images shows the increase in contrast and the resolution of substructures, especially in the macromolecular focal adhesion complexes to which the actin cables dock. At the higher resolution, the actin stress fiber in the focal adhesion ending appears to split to match rows of punctate zyxin structures (Fig. 5).

We corrected chromatic aberration using the ImageJ plugin bUnwarpJ (22). Images of whole cells of the same sample, acquired using an sCMOS camera, may be found in *CSD-ISM with an sCMOS Camera* (also see Fig. S4).

Fast 3D Imaging of Tau Protein. Tau is a neuronal microtubule-binding protein whose aggregation in Alzheimer's disease is thought to contribute to cell toxicity and neuronal loss in the affected brain. The size and distribution of these aggregates might hold important clues to understanding the still poorly understood mechanism of toxicity. Three-dimensional CSD-ISM operates at the length scale at which aggregates may be studied for fragmentation or fusion, and for potential clearance routes using the autophagosomal or exosomal compartment. Using a genetic expression model based on full-length (441-aa) Tau that was structurally optimized for β-sheet formation by three amino acid modifications in the microtubule binding repeat (3PO-Tau), we imaged the formation of morphological aggregates in three dimensions. This mutant Tau rapidly forms aggregates with associated toxicity and pathological hallmarks of Alzheimer's disease (23, 24). To this end, GFP-fused 3PO-Tau was expressed in N1E115 neuroblastoma cells, and the GFP label was imaged using CSD-ISM. Volume rendering of aggregated Tau in a selection of the cell shows the increased level of detail that may be observed (Fig. 6) with CSD-ISM. Each of

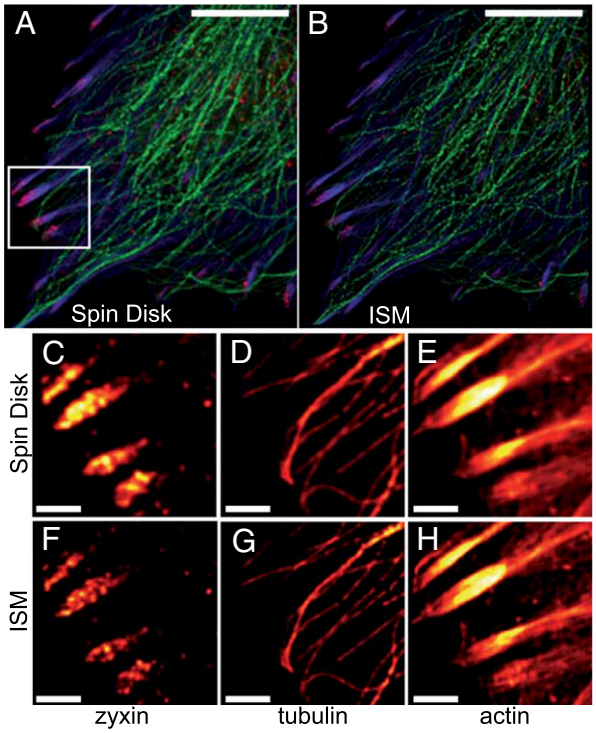

Fig. 5. ISM allows higher resolution in multicolor imaging. Multicolor ISM of fixed REF52 cells showing Alexa 488-labeled actin (blue) and TRITC-labeled tubulin (green) cytoskeletal networks together with the Alexa 647-labeled focal adhesion protein zyxin (red). A confocal image is shown in *A*. The corresponding CSD-ISM image from 378 single images is shown in *B*. For CSD-ISM images of Alexa 488 and TRITC, each single image was exposed for 66 μs (~15 s acquisition time), and for Alexa 647 an exposure of 210 μs (~45 s acquisition time) was used. Magnifications of the indicated regions of interest are shown in *C–H*. The scale bars are 10 μm for the overview and 2 μm for the regions of interest.

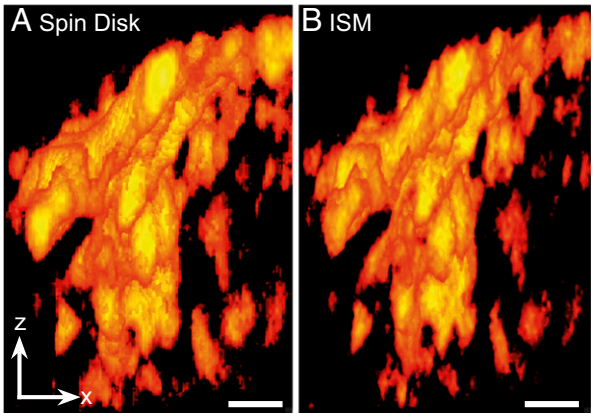

Fig. 6. ISM gives enhanced resolution in three dimensions. Three-dimensional representation of confocal (*A*) and CSD-ISM (*B*) *z*-stack data of GFP-fused 3PO-Tau aggregates in an N1E115 neuroblastoma cell. The increased level of detail in the ISM data allows for better characterization of different types and progression of aggregates. The data were acquired using the 16-pulse laser sequence (*Synchronization and Data Acquisition*). The images were calculated from 125 single images with an exposure time of 6 μs per image (~0.8 s acquisition time). The scale bar (1 μm) is the same for *x*- and *z*-direction. A movie of these data may be found as Movie S1.

the 85 CSD-ISM images in the stack was acquired within 1 s, demonstrating that superresolution images can be obtained on a sufficiently short time scale for biological imaging. A maximum-intensity projection movie of this data after 3D deconvolution may be found as Movie S1. For details, see *Fast 3D Imaging of Tau Protein*.

Four-Color 3D Imaging. Three-dimensional and multicolor imaging capabilities can be combined in CSD-ISM. Four-color 3D stacks of HeLa cells were acquired using the commonly used organelle stains Hoechst 33258 and MitoTracker M-7510, together with Alexa 488-labeled α-tubulin and Alexa 633-labeled Nup358, a protein of the NPC (25, 26). Images and 3D-projection movies may be found in *Four-Color 3D Imaging*, Movie S2, and Fig. S5. The ability to use commonly used fluorophores from selective organic stains to typical immunostaining labels and fluorescent proteins makes CSD-ISM a useful tool in cell biology. The morphology of a cell and its organelles can be evaluated in greater detail compared with the currently used routine fluorescence microscopy technique with highest resolution: confocal microscopy. The examples have shown that new biological information lies in the resolution window just beyond confocal microscopy.

Discussion

Like existing SIM techniques, CSD-ISM can deliver superior image quality in resolution and contrast compared with confocal imaging. We see its significant advantage over other techniques in its straightforward implementation, potentially opening up superresolution imaging capabilities to all camera-based confocal microscopy users. An existing confocal spinning-disk setup can be upgraded easily for ISM by modulating the laser light and synchronizing the spinning disk with the illumination and imaging camera. Modulation of any laser can be achieved using an AOTF, and here we have shown the performance of such a device for CSD-ISM. The synchronization with lasers and camera of the Yokogawa CSU-X1, which is used in most commercially available spinning-disk systems, is achieved simply by using an FPGA and the readily accessible trigger signals the CSU-X1 generates. The optical resolutions we could achieve using this system compare remarkably well with theoretical predictions. The lateral resolution and optical sectioning ability of the CSD-ISM approach the theoretical limit for any far-field microscope using linear optics, such as SIM, multifocal SIM, and related techniques.

Besides single-molecule measurements for evaluation of the improved resolution, we have demonstrated the capabilities of our method by imaging various biological systems. CSD-ISM does not put any restrictions on the used fluorophores, allowing its use in any experiment that is also accessible to normal wide-field or confocal fluorescence imaging. The fluorophores we used span the range from commonly used specific stains for organelles and subcellular structures, such as Hoechst for the nucleus, MitoTracker for mitochondria, and phalloidin for the actin cytoskeleton, to conventional fluorescent labels such as Alexa dyes, rhodamine, and fluorescent proteins (GFP).

We anticipate that the exceptional ease of use of CSD-ISM, its robustness, and its versatility, will make it a commonly used tool in the life sciences.

Methods

Microscopy System. Data acquisition was performed on an Olympus IX-71 microscope with a Yokogawa CSU-X1 (M1N-E) mounted to the left side port. The objective used was an Olympus 100× UAPON, N.A. 1.49. The dichroic mirror in the spinning-disk unit was a Di01-T405/488/568/647 from Semrock Inc. As emission filters, either a quad-band filter (BrightLine HC 446/523/600/677; Semrock) or individual bandpass filters (593-40, 525-45, 685-70, 447-60 BrightLine HC; Semrock) were used. After the spinning-disk unit, a telescope system for doubling the magnification (MAP1075150-A achromatic matched pair doublet; Thorlabs) was introduced to decrease the effective pixel size of the EM CCD camera [iXon ×3–897D (Andor Technology) with 512 × 512 pixels and 16-μm pixel size). The magnification of the objective, 1.2× magnification of the spinning-disk camera adapter, and 2× magnification before the camera resulted in an effective pixel size of 67 nm. Alternatively, an sCMOS camera [Neo (Andor Technology), 2,560 × 2,160 pixels, 6.5-μm pixel size] was mounted after the spin-disk unit.

Laser light (400, 488, 561, or 647 nm) was coupled into the CSU-X1 with an optical fiber. For illumination, the following laser sources were used: for 400 nm, a Cube 405–100C, 60 mW (Coherent); for 488 nm, a PhoxX 488–60, 60 mW; and for 647 nm, a PhoxX 647–147, 140 mW (Omicron Laserage). For illumination at 561 nm, a Cobolt Jive, 50 mW (Cobolt), modulated by an AOTFnC-400.650-TN (AA Optoelectronic) was used.

For 3D scanning, a PIFOC P725-2DC with E709-CRD controller from Physik Instrumente (PI) GmbH & Co. KG was used.

Stroboscopic Laser Excitation. Details on the synchronization of the CSD with the laser illumination and the camera using an FPGA may be found in *Synchronization and Data Acquisition*. Briefly, one ISM image was divided into typically 250 single camera exposures. A trigger signal from the CSU-X1 was used to modulate the laser and to time the camera exposure. After each of the 250 single images, the laser pulses were offset in time to achieve an offset in space as the disk spun, which accomplished scanning of the sample. Four laser pulses per offset were used, which produced four times as many spots on the camera image. These spots did not overlap. The *x*-distance between spots between shots was about 100 nm. The *y*-distance between spots (after the next row was at same *x*-position) was about 66 nm. For most images shown here, each shot was averaged over 23 cycles of the CSD, which corresponds to an acquisition time of 20 s for one CSD-ISM image. For all images recorded, the software waited for one trigger from the spin disk before starting the next cycle.

Image Calculation and Analysis. The calculation of the CSD-ISM image from the raw data stack, as well as the Fourier reweighting of the resulting image, was performed using Matlab (The MathWorks Inc.). For the Fourier reweighting, optical transfer functions were calculated using the wave optical theory by Wolf (27) and Richards and Wolf (28). The positions of the pinholes of the CSD were determined using rapidSTORM 3.2 software (29) with maximum likelihood estimator (MLE) improvement of the fit. Details of the image calculation are described in *ISM Algorithm and Image Calculation Using Matlab*. An ImageJ plugin for calculation of the CSD-ISM image from raw data and reference data may be found on our Web site under www.joerg-enderlein.de/ISM along with sample datasets.

Nuclear pore density was measured with the ITCN ImageJ plugin, which finds the peak fluorescence intensity of each pore in a manually selected area on the nuclear envelope of seven samples for each method. For the spinning-disk samples, the parameters were set as follows: width of four pixels,

minimum distance of five pixels, and a threshold of 1.0. With a twofold resolution enhancement, the parameters for the ISM samples were adjusted as follows: width of eight pixels, minimum distance of six pixels, and a threshold of 0.5. Errors for peak detection were tested manually (spin disk, maximum 4%; ISM, maximum 9%). In two of seven samples, the NPC density was measured from images in which NPCs were labeled with Alexa 568. An example of the NPC density measurements may be found in *Measurement of Nuclear Pore Complex Density* (Fig. S6).

Sample Preparation. ***Atto 655 single-molecule samples.*** For recording images of single fluorescent molecules on a glass surface, cover slides were cleaned by ultrasonication in acetone, ethanol, and ultrapure water. Single molecules of Atto 655 on glass were prepared by drying a very dilute solution onto a cleaned glass cover slide. The concentration of the dye was adjusted to result in a surface density of molecules in which individual molecules could be distinguished clearly. The samples were imaged without any further treatment.
NPC samples. HeLa s/a cells (14) were maintained in DMEM (GlutaMAX; Invitrogen) supplemented with 10% (vol/vol) FCS (Gibco) under 5% CO_2 at 37 °C. For staining, cells were seeded onto 12-mm poly-L-lysine–coated (Sigma) coverslips and incubated until they reached 50% cell density. The sample was washed with PBS, fixed with 3.7% (vol/vol) formaldehyde in PBS, and permeabilized with 0.5% Triton X-100 in PBS for 5 min. After washing, the sample was blocked with 10% (wt/vol) BSA in PBS for 30 min and incubated with mAb414 (Sigma; 1.5 μg/mL) diluted in PBS with 1% (wt/vol) BSA for 2 h. The sample was rinsed with PBS three times and incubated with the secondary antibody (goat anti-mouse Alexa 488, 4 μg/mL; Molecular Probes) diluted in PBS with 1% (wt/vol) BSA for 2 h. After the final washing step, the sample was mounted in Aqua-Poly/Mount (Polyscience) and sealed with nail polish.
Cytoskeletal and focal adhesion samples. REF52 cells were cultured in DMEM supplemented with GlutaMAX and 10% (vol/vol) FCS in a humidified atmosphere of 5% CO_2. For microscopy, cells were plated on fibronectin-coated (10 μg/mL) coverslips and grown to a confluency of 40–50%. Cells were fixed with 4% (vol/vol) formaldehyde, quenched with 100 mM glycine in PBS, and permeabilized with 0.1% Triton X-100 in PBS. Blocking, washing, and antibody incubations were performed using 0.2% gelatin in PBS. Tubulin and zyxin proteins were detected using the monoclonal anti–α-tubulin (Clone DM1A; Sigma) antibody at a dilution of 1:250 and the polyclonal antizyxin antibody (Sigma) at a dilution of 1:400, respectively. TRITC-conjugated goat anti-mouse and Alexa Fluor 647-conjugated goat anti-rabbit secondary antibodies (both minimized for cross-reactivity; Jackson ImmunoResearch Laboratories) were used for visualization. The actin cytoskeleton was stained using phalloidin–Alexa 488 (Invitrogen) in a dilution of 1:200. Cells were mounted in Mowiol. The images of actin filaments shown in Figs. 1 and 2 were prepared in the same fashion.
Tau protein samples. N1E115 neuroblastoma cells were cultured in DMEM supplemented with 10% (vol/vol) FCS in a humidified atmosphere of 5% CO_2. Cells were plated on coverslips, grown to a confluency of 60–70%, and transfected with GFP-3PO-Tau using Lipofectamine LTX (Invitrogen) according to the manufacturer's instructions. After 24 h of expression, cells were fixed in 4% (vol/vol) formaldehyde, quenched with 100 mM glycine in PBS, and washed with PBS before mounting in Mowiol.
Four-color samples. HeLa P4 cells (31) were grown in DMEM (1X; Gibco) supplemented with 10% (vol/vol) calf serum (Gibco), 100 U/mL penicillin, 100 μg/mL streptomycin, and 2 mM L-glutamine (Gibco) under 5% CO_2 at 37 °C. For staining, cells were seeded onto poly-L-lysine–coated (Sigma) 12-mm coverslips and incubated until they reached 50% confluency. Cells were incubated with 20 ng/mL MitoTracker (M-7510; Invitrogen) for 15 min, washed with PBS, fixed with 3.7% (vol/vol) formaldehyde in PBS, and permeabilized with 0.5% Triton X-100 in PBS for 5 min. After washing, the samples were blocked with 2% (wt/vol) BSA in PBS for 30 min and incubated with rabbit anti–α-tubulin (111224-AP; Proteintech) and goat anti-Nup358 (25, 26) diluted in PBS with 2% (wt/vol) BSA for 1 h. The samples were rinsed three times with PBS and incubated with secondary antibodies (donkey anti-rabbit Alexa 488 and donkey anti-goat Alexa 633, 4 μg/mL; Molecular Probes) diluted in PBS with 1% (wt/vol) BSA for 1.5 h. DNA was stained with Hoechst 33258 (Molecular Probes). After the final washing step, samples were mounted in mounting medium (Dako).

ACKNOWLEDGMENTS. We thank Dr. Alexey Chizhik for his kind help with the schematic drawing of the setup and ISM principle. We also thank Katrina Don Paul for technical assistance with sample preparations. This work was supported by the Deutsche Forschungsgemeinschaft Cluster of Excellence "Center for Nanoscale Microscopy and Molecular Physiology of the Brain." M.C. thanks the Dorothea Schlözer Programme of the Georg-August-University Göttingen for support.

1. Hell SW, Wichmann J (1994) Breaking the diffraction resolution limit by stimulated emission: Stimulated-emission-depletion fluorescence microscopy. *Opt Lett* 19(11): 780–782.
2. Betzig E, et al. (2006) Imaging intracellular fluorescent proteins at nanometer resolution. *Science* 313(5793):1642–1645.
3. Rust MJ, Bates M, Zhuang X (2006) Sub-diffraction-limit imaging by stochastic optical reconstruction microscopy (STORM). *Nat Methods* 3(10):793–795.
4. Müller CB, Enderlein J (2010) Image scanning microscopy. *Phys Rev Lett* 104(19): 198101.
5. Gustafsson MG (2000) Surpassing the lateral resolution limit by a factor of two using structured illumination microscopy. *J Microsc* 198(Pt 2):82–87.
6. York AG, et al. (2012) Resolution doubling in live, multicellular organisms via multifocal structured illumination microscopy. *Nat Methods* 9(7):749–754.
7. Gustafsson MGL, Agard DA, Sedat JW (1999) I5M: 3D widefield light microscopy with better than 100 nm axial resolution. *J Microsc* 195(Pt 1):10–16.
8. Sheppard CJR (1988) Super-resolution in confocal imaging. *Optik (Stuttg)* 80:53–54.
9. Van der Voort HTM, Brakenhoff GJ (1990) 3-D image formation in high-aperture fluorescence confocal microscopy: A numerical analysis. *J Microsc* 158:43–54.
10. Schulz O, et al. (2013) Tip induced fluorescence quenching for nanometer optical and topographical resolution. *Optical Nanoscopy* 2:1.
11. Lucy L (1974) An iterative technique for the rectification of observed distributions. *Astron J* 79:745–754.
12. Richardson WH (1972) Bayesian-based iterative method of image restoration. *J Opt Soc Am* 62(1):55–59.
13. Sarder P, Nehorai A (2006) Deconvolution methods for 3-D fluorescence microscopy images. *IEEE Signal Process Mag* 23:32–45.
14. Weidenfeld I, et al. (2009) Inducible expression of coding and inhibitory RNAs from retargetable genomic loci. *Nucleic Acids Res* 37(7):e50.
15. Grossman E, Medalia O, Zwerger M (2012) Functional architecture of the nuclear pore complex. *Annu Rev Biophys* 41:557–584.
16. Wozniak R, Burke B, Doye V (2010) Nuclear transport and the mitotic apparatus: An evolving relationship. *Cell Mol Life Sci* 67(13):2215–2230.
17. Hetzer MW (2010) The role of the nuclear pore complex in aging of post-mitotic cells. *Aging (Albany, NY Online)* 2(2):74–75.
18. Maimon T, Elad N, Dahan I, Medalia O (2012) The human nuclear pore complex as revealed by cryo-electron tomography. *Structure* 20(6):998–1006.
19. Beck M, Lucić V, Förster F, Baumeister W, Medalia O (2007) Snapshots of nuclear pore complexes in action captured by cryo-electron tomography. *Nature* 449(7162): 611–615.
20. Löschberger A, et al. (2012) Super-resolution imaging visualizes the eightfold symmetry of gp210 proteins around the nuclear pore complex and resolves the central channel with nanometer resolution. *J Cell Sci* 125(Pt 3):570–575.
21. Maeshima K, et al. (2006) Cell-cycle-dependent dynamics of nuclear pores: pore-free islands and lamins. *J Cell Sci* 119(Pt 21):4442–4451.
22. Arganda-Carreras I, et al. (2006) Consistent and elastic registration of histological sections using vector-spline regularization. *Computer Vision Approaches to Medical Image Analysis*, eds Beichel R, Sonka M (Springer, Berlin), pp 85–95.
23. Dassie E, et al. (2013) Focal expression of adeno-associated viral-mutant tau induces widespread impairment in an APP mouse model. *Neurobiol Aging* 34(5):1355–1368.
24. Iliev AI, Ganesan S, Bunt G, Wouters FS (2006) Removal of pattern-breaking sequences in microtubule binding repeats produces instantaneous tau aggregation and toxicity. *J Biol Chem* 281(48):37195–37204.
25. Pichler A, Gast A, Seeler JS, Dejean A, Melchior F (2002) The nucleoporin RanBP2 has SUMO1 E3 ligase activity. *Cell* 108(1):109–120.
26. Hutten S, Flotho A, Melchior F, Kehlenbach RH (2008) The Nup358-RanGAP complex is required for efficient importin alpha/beta-dependent nuclear import. *Mol Biol Cell* 19(5):2300–2310.
27. Wolf E (1959) Electromagnetic diffraction in optical systems. I. An integral representation of the image field. *Proc R Soc Lond A* 253(1274):349–357.
28. Richards B, Wolf E (1959) Electromagnetic diffraction in optical systems. II. Structure of the image field in an aplanatic system. *Proc R Soc Lond A* 253(1274):358–379.
29. Wolter S, et al. (2010) Real-time computation of subdiffraction-resolution fluorescence images. *J Microsc* 237(1):12–22.
30. Charneau P, et al. (1994) HIV-1 reverse transcription. A termination step at the center of the genome. *J Mol Biol* 241(5):651–662.

Supporting Information

Schulz et al. 10.1073/pnas.1315858110

Theory of Image-Scanning Microscopy

Let us first shortly recall image formation in a conventional wide-field and in a confocal microscope. In a wide-field microscope with homogeneous illumination of the sample, the image $I(\mathbf{s})$, which is the intensity at pixel position $\mathbf{s}$ on the CCD of the imaging camera, is given by

$$I(\mathbf{s}) = \int d\mathbf{r}' D(\mathbf{s}-\mathbf{r}') S(\mathbf{r}'),$$

where $D(\mathbf{s}-\mathbf{r}')$ is the point-spread function (PSF) of the wide-field microscope describing the intensity generated at position $\mathbf{s}$ on the CCD by a point emitter at position $\mathbf{r}'$ in the sample, and $S(\mathbf{r}')$ is the sample function describing the density of emitters at position $\mathbf{r}'$ in the sample. Knowing the PSF, the optical transfer function (OTF) for wide-field imaging is simply the Fourier transform of $D(\mathbf{s}-\mathbf{r}')$. Here and below, we assume that the image coordinate $\mathbf{s}$ is given in normalized units corresponding to a 1:1 image magnification (back projection of the image into sample space). Without restriction of generality, this significantly simplifies all the ensuing mathematics.

The situation becomes more complex for a confocal microscope, which scans the sample with a focused laser beam and detects the fluorescence by focusing it through a confocal circular pinhole onto a point detector (avalanche photodiode or photomultiplier tube). Let the light intensity distribution in the focus be $E(\mathbf{r}-\mathbf{r}')$, which is a function of the distance between the point of interest, $\mathbf{r}'$, and the center position of the focus, $\mathbf{r}$. Then, the image of the confocal microscope is given by

$$I(\mathbf{r}) = \int d\mathbf{s} \int d\mathbf{r}' A(\mathbf{s}) D(\mathbf{s}-\mathbf{r}'+\mathbf{r}) E(\mathbf{r}-\mathbf{r}') S(\mathbf{r}').$$

Here, D and S have the same meaning as before, but $A(\mathbf{s})$ describes the action of the confocal aperture and is given by

$$A(\mathbf{s}) \equiv A(s) = \begin{cases} 1 & \text{if} \quad s < a \\ 0 & \text{if} \quad s > a \end{cases},$$

where a is the radius of the confocal aperture when back-projected into sample space. We can define the PSF $U_{con}(\mathbf{r})$ of this confocal microscope via

$$I(\mathbf{r}) = \int d\mathbf{r}' U_{con}(\mathbf{r}-\mathbf{r}') S(\mathbf{r}')$$

so that one has

$$U_{con}(\mathbf{r}) = \int d\mathbf{s} A(\mathbf{s}) D(\mathbf{s}+\mathbf{r}) E(\mathbf{r}).$$

By replacing the functions D and E by their Fourier transforms, one finds

$$U_{con}(\mathbf{r}) = \int d\mathbf{s} \int d\mathbf{k} \int d\mathbf{k}' A(\mathbf{s}) \tilde{D}(\mathbf{k}') e^{i\mathbf{k}'\cdot(\mathbf{s}+\mathbf{r})} \tilde{E}(\mathbf{k}) e^{i\mathbf{k}\cdot\mathbf{r}},$$

where a tilde here denotes the Fourier transform of the corresponding function. Now, the integration over $\mathbf{s}$ can be performed explicitly, yielding

$$\int d\mathbf{s} A(\mathbf{s}) e^{i\mathbf{k}\cdot\mathbf{s}} = \int_0^a ds s \int_0^{2\pi} d\phi e^{iqs\cos\phi} = 2\pi \int_0^a ds s J_0(qs) = \frac{2\pi a}{q} J_1(qa).$$

Here, the J_n denote Bessel functions of the first kind of order n. Thus, one finds up to a constant prefactor,

$$U_{con}(\mathbf{r}) = \int d\mathbf{k} e^{i\mathbf{k}\cdot\mathbf{r}} \left[\int d\mathbf{k}' \frac{J_1(aq')}{q'} \tilde{D}(\mathbf{k}') \tilde{E}(\mathbf{k}-\mathbf{k}') \right],$$

and correspondingly for the OTF,

$$\tilde{U}_{con}(\mathbf{k}) = \int d\mathbf{k}' \frac{J_1(aq')}{q'} \tilde{D}(\mathbf{k}') \tilde{E}(\mathbf{k}-\mathbf{k}').$$

Here, we restrict ourselves to the case that both the excitation intensity profile $E(\mathbf{r})$ and the wide-field PSF $D(\mathbf{r})$ are symmetric functions with respect to the optical axis; then, one also has $\tilde{D}(\mathbf{k}) = \tilde{D}(q,w)$ and $\tilde{E}(\mathbf{k}) = \tilde{E}(q,w)$, where q is the radial Fourier coordinate perpendicular to the optical axis and w is the axial Fourier coordinate parallel to the optical axis. In that case, one may use a Hankel transform to represent both $J_1(aq)\tilde{D}(q,w)/q$ and $\tilde{E}(q,w)$ in the form

$$\frac{J_1(aq)\tilde{D}(q,w)}{q} = \int_0^\infty d\xi\, \xi\, \tilde{\tilde{F}}(\xi,w) J_0(q\xi)$$

and

$$\tilde{E}(q,w) = \int_0^\infty d\xi\, \xi \tilde{\tilde{E}}(\xi,w) J_0(q\xi),$$

where we have introduced the Hankel transforms $\tilde{\tilde{F}}$ and $\tilde{\tilde{E}}$, which themselves are given by

$$\tilde{\tilde{F}}(\xi,w) = \int_0^\infty dq\, J_1(aq) \tilde{D}(q,w) J_0(q\xi)$$

and

$$\tilde{\tilde{E}}(\xi,w) = \int_0^\infty dq q \tilde{E}(q,w) J_0(q\xi).$$

Inserting these representations in the equation for $\tilde{U}_{con}$ yields

$$\tilde{U}_{con}(\mathbf{k}) = \int_0^\infty dq' q' \int_{-\infty}^\infty dw' \int_0^{2\pi} d\psi \int_0^\infty d\xi' \xi' \int_0^\infty d\xi \xi \tilde{\tilde{F}}(\xi',w') J_0(\xi' q') \tilde{\tilde{E}}(\xi, w-w') J_0\left(\xi\sqrt{q^2+q'^2-2qq'\cos\psi}\right).$$

Now, one may use Graf's addition theorem

$$J_0(|\mathbf{u}+\mathbf{v}|) = \sum_{n=-\infty}^{\infty} J_n(|\mathbf{u}|) J_n(|\mathbf{v}|) \cos(n\varphi)$$

where $\mathbf{u}$ and $\mathbf{v}$ are two vectors and ϕ is the angle between them. This can be used to expand the last Bessel function in the

above integral and then to perform the integration over ψ. Then one finds

$$\tilde{U}_{con}(\mathbf{k}) = \int_0^\infty dq'q' \int_{-\infty}^{\infty} dw' \int_0^\infty d\xi'\xi' \int_0^\infty d\xi\xi \tilde{\tilde{F}}(\xi', w') J_0(\xi' q') \tilde{\tilde{E}}(\xi, w - w') J_0(\xi q) J_0(\xi q').$$

Using also the orthogonality relation for Bessel functions,

$$\int_0^\infty dq\, q J_0(q\xi') J_0(q\xi) = \frac{\delta(\xi - \xi')}{\xi},$$

the expression for the OTF simplifies further to

$$\tilde{U}_{con}(q, w) = \int_{-\infty}^{\infty} dw' \int_0^\infty d\xi\xi\, \tilde{\tilde{F}}(\xi, w') \tilde{\tilde{E}}(\xi, w - w') J_0(\xi q).$$

The PSF is obtained by a Fourier–Hankel back transformation of this OTF.

In image scanning microscopy (ISM), the point detector of a conventional confocal microscope is replaced by an imaging detector so that at each scan position, an image of the illuminated region is recorded. Thus, the raw data of an ISM image have the form

$$I(\mathbf{r}, \mathbf{s}) = \int d\mathbf{r}' A(\mathbf{s}) D(\mathbf{s} - \mathbf{r}' + \mathbf{r}) E(\mathbf{r} - \mathbf{r}') S(\mathbf{r}'),$$

where **r** denotes the scan position and **s** the position on the imaging CCD. When integrating $I(\mathbf{r}, \mathbf{s})$ over **s**, one recovers the image as obtained by the confocal microscope. One also might first shift the data in **r**-space by an amount of –**s** and then integrate over **s**, which would recover the image as obtained by a pure wide-field microscope. As visualized in Fig. 1*B* in the main text, the expression $D(\mathbf{s} - \mathbf{r}' + \mathbf{r}) E(\mathbf{r} - \mathbf{r}')$ is the product of the excitation intensity distribution E with the shifted PSF for wide-field imaging (shifted by an amount –**s**). If one neglects the Stokes shift between excitation and emission wavelength so that $D(\mathbf{r}) = E(\mathbf{r})$, then the center of gravity of the product $D(\mathbf{s} - \mathbf{r}' + \mathbf{r}) E(\mathbf{r} - \mathbf{r}')$ is shifted by an amount –**s**/2 from the optical axis. The idea of ISM is to shift this center of gravity back toward the optical axis, i.e., by +**s**/2, and only then to integrate over **s**. The result is

$$I_{ISM}(\mathbf{r}) = \int d\mathbf{s}\, I\left(\mathbf{r} - \frac{\mathbf{s}}{2}, \mathbf{s}\right) = \int d\mathbf{r}' \int d\mathbf{s}\, A(\mathbf{s}) D\left(\mathbf{r} - \mathbf{r}' + \frac{\mathbf{s}}{2}\right) E\left(\mathbf{r} - \mathbf{r}' - \frac{\mathbf{s}}{2}\right) S(\mathbf{r}')$$

so that the PSF of ISM is given by

$$U_{ISM}(\mathbf{r}) = \int d\mathbf{s}\, A(\mathbf{s}) D\left(\mathbf{r} + \frac{\mathbf{s}}{2}\right) E\left(\mathbf{r} - \frac{\mathbf{s}}{2}\right).$$

This shift and integration means that light recorded at pixel position **s** with the scan focus at position **r** is added to the final image at position **r** + **s**/2. This may be done either by shrinking the CCD image taken at one scan position by a factor of two and then adding this shrunken image at center position **r** to the final image or by taking the CCD image recorded at scan position **r** as it is and then adding it at center position 2**r** to the final image. In the latter case, one has to rescale the final image by one half after the ISM procedure is completed. In our implementation of ISM with a spinning-disk confocal microscope, we use the latter option, which is much less demanding computationally and extremely simple. The implementation using Matlab is outlined in *ISM Algorithm and Image Calculation Using Matlab*.

For explicitly calculating the PSF and OTF of ISM, one again may use the axial symmetry of both D and E to reduce the 3D integral to a 2D one. First, one expresses both D and E by their Hankel transforms,

$$D(\mathbf{r}) = D(\rho, z) = \int dq\, q\, \tilde{D}(q, z) J_0(q\rho)$$

and

$$E(\mathbf{r}) = E(\rho, z) = \int dq\, q\, \tilde{E}(q, z) J_0(q\rho).$$

Again using Graf's addition theorem and integrating over **s** one finds

$$U_{ISM}(\rho, z) = 4\pi \int dqq \int dq'q'\, \tilde{D}(q, z) R(q, q', \rho) \tilde{E}(q', z),$$

where the kernel function

$$R(q, q', \rho) = \sum_{n=0}^{\infty} \frac{(-1)^n a J_n(q\rho) J_n(q'\rho) \left[q' J_n(qa/2) J_{n-1}(q'a/2) - q J_{n-1}(qa/2) J_n(q'a/2)\right]}{q^2 - q'^2}$$

was introduced, which takes, in the limit $q' \to q$, the value

$$R(q, q, \rho) = \sum_{n=0}^{\infty} \frac{(-1)^n a^2 J_n(q\rho) J_n(q'\rho) \left[J_n^2(qa/2) - J_{n-1}(qa/2) J_{n+1}(qa/2)\right]}{4}.$$

The OTF finally is obtained by a Fourier–Hankel transform of the PSF.

Finally, we have to specify the excitation intensity distribution $E(\mathbf{r})$ and the PSF of wide-field imaging $D(\mathbf{r})$. In the scalar approximation (neglecting the vector character and polarization of the electromagnetic field), the light intensity distribution generated by focusing a plane wave through a perfect objective with maximum light collection angle Θ is given by

$$E(\rho, z) \propto \left| \int_0^{\Theta} d\theta \sqrt{\cos\theta} \sin\theta \exp(ikz\cos\theta) J_0(k\rho\sin\theta) \right|^2,$$

where $k = 2\pi n/\lambda$ is the wave number of light with vacuum wavelength λ inside the objective's immersion medium of refractive index n. As already mentioned above, under ideal conditions and while neglecting any Stokes shift between excitation and detection wavelengths, the PSF for wide-field imaging $D(\mathbf{r})$ is identical to $E(\mathbf{r})$.

We performed numerical calculations for an excitation (detection) wavelength of 500 nm, assuming a confocal pinhole diameter of 500 nm (back projection in sample space), and a maximum angle of light collection and focusing corresponding to a numerical aperture of the objective of 1.2 and a refractive index of the objective's immersion medium of 1.33 (water). Fig. S1 compares the resulting OTFs for a wide-field microscope, the conventional confocal microscope, and the ISM microscope with pinhole. The green solid line denotes the limits of the support of the maximally extended OTF, which is obtained by an autoconvolution of the OTF of the wide-field microscope, which corresponds to the support of the OTF of a hypothetical confocal microscope with zero-size pinhole. This also is the maximum possible support an OTF can have for any diffraction-limited optical microscope.

Fourier Reweighting

Although the OTF of an ISM nearly completely fills the whole frequency range maximally accessible by a diffraction-limited microscope, the amplitude distribution of its OTF is not optimal. We will demonstrate this by a simplified discussion of the imaging properties of ISM for objects within the focal plane of the microscope. In this case, we assume that the confocal aperture of the microscope does not significantly restrict light detection laterally, i.e., perpendicular to the optical axis, so that the PSF of an ISM simplifies to

$$U_{ISM}(\boldsymbol{\rho}) \approx \int d\mathbf{s}\, D\left(\boldsymbol{\rho} + \frac{\mathbf{s}}{2}\right) E\left(\boldsymbol{\rho} - \frac{\mathbf{s}}{2}\right),$$

where $\boldsymbol{\rho}$ is the lateral scan position perpendicular to the optical axis (i.e., here we strictly consider imaging from the focal plane of the objective into the conjugate plane of the CCD). Thus, we assume that the excitation intensity distribution (as well as the wide-field imaging PSF) has fallen off to negligible values before the presence of the confocal aperture makes itself tangible. This approximation tremendously simplifies the (lateral) OTF of the ISM system, which now reads

$$\tilde{U}_{ISM}(\mathbf{q}) \approx \tilde{D}\left(\frac{\mathbf{q}}{2}\right)\tilde{E}\left(\frac{\mathbf{q}}{2}\right) \approx \tilde{D}^2\left(\frac{\mathbf{q}}{2}\right).$$

From this expression, it clearly is visible that the support of the OTF of an ISM is approximately twice as large as the support of the original wide-field PSF (or of the Fourier transform of excitation intensity distribution), which signifies a doubled lateral resolution. However, the ideal OTF for a microscope with doubled resolution would not be $\tilde{D}^2(\mathbf{q}/2)$ but $\tilde{D}(\mathbf{q}/2)$. Thus, the OTF of an ISM overweighs components of the OTF with large amplitude (small values of $|\mathbf{q}|$) and underweighs components with small amplitude (large values of $|\mathbf{q}|$). A naïve approach would be to reweigh the Fourier transform of an obtained ISM image with the weight function $\tilde{D}^{-1}(\mathbf{q}/2)$, which, however, is dangerous because $\tilde{D}(\mathbf{q})$ falls off to zero toward the edge of its support. Thus, we instead use as a weight function

$$\tilde{W}(\mathbf{q}) = \frac{1}{\tilde{D}(\mathbf{q}/2) + \varepsilon}$$

with a small normalizing parameter ε, which should be by one order or more smaller than the maximum amplitude of $|\tilde{D}(\mathbf{q})|$. This prevents the amplification of image noise at high frequencies in Fourier space. Fig. S2 compares the PSFs of the wide-field microscope, the confocal microscope, and the Fourier-reweighted ISM, demonstrating the reduction in extent of the PSF from wide-field microscope to ISM. The $1/e^2$ widths of the three distributions are 222 nm for the wide-field microscope, 198 nm for the confocal microscope, and 128 nm for the ISM with Fourier reweighting.

ISM Algorithm and Image Calculation Using Matlab

The data recorded in one-focus ISM as described in ref. 1 are four-dimensional: at each position of the scan–focus, one records a 2D image of the illuminated region so that one finally obtains data depending on both the relative position of the focus in the sample and the 2D pixel positions on the camera. Then, to calculate the ISM image, one shifts each pixel halfway toward the optical before registering it at the current scan position. In confocal spinning-disk ISM (CSD-ISM), however, there are multiple scanning foci corresponding to the microlenses and pinholes in the Nipkow disk. Before we can apply the pixel reassignment of the ISM data, we need to know their position. This is achieved by imaging a uniformly fluorescing sample in ISM mode (stroboscopic illumination). Then, for each image in a sequence, the position of the spots is determined using the rapidSTORM software (version 3.2) (2).

After finding the center positions of the foci for each frame, a Matlab script is used to calculate the ISM image from the raw data. First, the coordinates of the foci are loaded and adjusted to an image size that in both dimensions is 10 times that of the final ISM image. Enlarging the image matrix in this fashion accounts for the fact that the focus centers are not necessarily in the center of a pixel. Now, for every frame in the sequence, and for every focus position in the image, the raw data from a square area around the pinhole coordinate are copied to the final image matrix at a position with the coordinates multiplied by two. This procedure corresponds to moving the information from each pixel half its distance to the optical axis. The size of the area from which the data are taken (window) is three times the width of a Gaussian fit to a spot in the reference data, or in Matlab code:

```
Final_image(2*yc + window, 2*xc + window)
= Final_image(2*yc + window, 2*xc + window)
+ ((raw_data(yc + window, xc + window)) - background).
```

Here, the indices for number of image and pinhole position have been omitted; xc and yc are the pinhole coordinates; and background is the readout noise of the camera. If the position of the pinhole is too close to the edge of the image, such that the square from which data are taken would be outside the image, it is discarded. After summing over all images and pinhole positions, the final image is reduced by a factor of 10. On this final image, the Fourier reweighting as described before is performed.

A CSD-ISM image calculation plugin for ImageJ may be found on our Web site (www.joerg-enderlein.de/ISM).

Synchronization and Data Acquisition

The core of the CSD microscope is composed of two rapidly and synchronously rotating disks, one with an array of microlenses and the other with a coaligned array of pinholes. These microlenses and pinholes are arranged in Archimedean spirals (Nipkow disk geometry), and repeat every 1/12th of disk rotation. The spin-disk unit is operated at a speed of 1,500 rpm so that the same focal spot arrangement repeats itself 300 times per second. At this speed, the laser pulses used for the stroboscopic illumination have to be short enough so that any elongation of the foci becomes negligible. We have chosen a pulse length of 6 μs because at about 8 μs pulse length, focal spot asymmetry becomes discernible. The microlenses/pinholes on the spin disk are relatively far apart to prevent excessive cross-talk between focal spots during image acquisition (detection of fluorescence excited in one focus through a pinhole associated with another focus). However, because we use stroboscopic illumination, we can increase the number of apparent spots by illuminating the sample more than once during one repetition period of the focal spot arrangement. For synchronizing the laser pulsing with the spin-disk rotation, we use the trigger signals generated by the spin-disk unit. A long trigger marks a full rotation of the disk, whereas 11 shorter triggers mark each additional image frame. The movement of the spin disk, the laser pulses, and the exposure of the camera are coordinated via a field-programmable gate array (FPGA; NI PCIe-7842R; National Instruments). The programming of the FPGA is realized using LabVIEW. As the disk rotates, the time T between each trigger is calculated. This time is used to calculate the laser trigger signals for the next frame. Explicitly, in cycle number n + 1, the period T(n) is divided into four equal parts to produce laser pulses at times 0, T(n)/4, T(n)/2, 3*T(n)/4 after the spin-disk trigger. In the next cycle, these times are augmented by a certain delay that, in effect, moves the focus pattern. The delays are calculated by dividing T(n) into 1,000 equal parts (Fig. S3). Using four pulses in one cycle, this corresponds to 250 steps for one full image acquisition. The camera exposure is triggered in synchronization with the laser pulses. The camera trigger is produced shortly after the last laser trigger in a cycle so that the readout sequence, which is at the beginning of a frame (frame transfer mode), is finished when the first laser pulse of a cycle starts. Using the four-pulse sequence, one full ISM image (250 steps) can be acquired within 1 s.

In addition to the 4-pulse sequence, a 16-pulse sequence may be used. An 8-pulse sequence is generated in a manner similar to that of the 4-pulse sequence, and it is duplicated by introducing a short delay (20 μs) to the triggers. In this illumination scheme, 125 images are used to create one full image within 0.5 s. However, for the 8- and 16-pulse sequences, the images of the foci start to overlap, causing slight artifacts in the final ISM image. Thus, using the 16-point illumination is a tradeoff between speed and image quality. In the Fourier reweighted image, however, the artifacts often are reduced and may be eliminated by Fourier filtering, with no obvious loss of information in the image.

The distance between spots of consecutive steps of the sequence is about 100 nm for a 250-image sequence (125-image sequence for 8- or 16-pulse sequences). The *y* distance between spots (after the next row is at the same *x* position) is about 66 nm (about 33 nm with 8- or 16-pulse sequence).

The camera trigger may be set to occur less frequently than once for every laser pulse sequence. In effect, the recording speed may be matched to the camera frame rate for larger areas of interest or to allow for a longer accumulation of light for obtaining a better signal-to-noise ratio. For most images recorded, the camera was triggered after 23 laser pulse cycles, corresponding to an acquisition time of 20 s for 250 images in a sequence. For all images recorded, the software waited for one trigger from the spin disk before starting the next cycle.

Because the triggers for both the laser and the camera are produced by the FPGA, which depends only on the input of the spin-disk trigger, the camera's operation does not depend on the use of special acquisition software; homemade solutions, as well as the manufacturer's control software, may be used. For data acquisition, we used a custom-made LabVIEW program, but we also tested the functionality of the spin-disk ISM using Andor's Solis software (*CSD-ISM with an sCMOS Camera*).

The four-pulse illumination sequence also may be used to introduce simultaneous multicolor imaging by routing the pulse trigger to four different lasers. In this fashion, the fluorescence excited by the different excitation wavelengths will be well separated on the camera chip. Because the CSD is synchronized with the lasers, the emission of a certain color will always appear on the same spot of the camera for a given image in the sequence. Taking reference data for each color individually, the data may be sorted and analyzed separately.

Signal Strength and Signal-to-Noise Ratio

To achieve the stroboscopic illumination, the laser pulses must be very short. In the case of a rotation of the disk at 1,500 rpm (12 images per full rotation, 300 images per second), we used a laser pulse length of 6 μs. This means that we effectively illuminated only about 1/555 of the time vs. continuous illumination. (This fraction does not change for faster rotation of the disk because in this case, the laser pulse length also has to be shortened to maintain the size of the foci.) For a sequence of 250 images, which may be calculated into the final ISM image, this means that the ISM image would be about 2.2 times dimmer than the fastest possible regular spinning-disk image (3.3 ms per frame). However, by using the four-pulse sequence, the shortest-acquisition-time ISM image is about 1.8 times brighter than the fastest possible spinning-disk image. For the Tau protein measurements (see Fast 3D Imaging of Tau Protein in the main text), the 16-pulse sequence was used, which increases the brightness by another factor of four. This means that within 1 s, an image about seven times brighter than the fastest possible regular CSD image can be recorded.

An important question is the signal-to-noise ratio of CSD-ISM in comparison with normal wide-field microscopy and structured illumination microscopy (SIM). Here, we refer to the work by Pitter and coworkers (3–5), who have given an excellent analysis of the impact of photon detection noise on the frequency spectrum of the OTF of various types of microscopes. In their publications, they show that a SIM system shows optimal performance in terms of signal-to-noise ratio across the Fourier spectrum of the OTF. In comparison, ISM is equivalent to a confocal microscope with infinitely small pinhole, which has a suboptimal signal-to noise ratio at larger spatial frequencies; see the detailed analysis and figures (especially figure 2) in ref. 3. The reason is that in SIM, the excitation intensity is modulated with the largest possible spatial frequency, whereas the laser focus of a confocal laser scanning system is a superposition of all possible spatial frequencies, leading to an overweighting of lower frequencies with respect to higher spatial frequencies. Thus, SIM shows a better signal-to-noise performance than ISM, but at the price of much higher technical complexity.

CSD-ISM with an sCMOS Camera

For most experiments, we chose the EM CCD over the sCMOS camera based on its superior sensitivity. The larger chip of the sCMOS, however, allows us to image the whole area illuminated by the CSD. For fixed samples, for which fast imaging is not crucial, one may integrate over many laser pulse cycles to get a better signal-to-noise ratio. Readout noise and the varying intensity-to-signal performance of every pixel were taken into account by subtracting a background image from each image of the ISM raw data stack. With our Neo sCMOS (2,560 × 2,160 pixels^2, 6.5-μm pixel size; Andor Technology), the area illumi-

nated by the spin disk corresponded to 2,048 × 1,461 pixels^2, or 111 × 79 μm^2. The data acquisition was performed using Andor Solis software in the "external exposure" trigger mode. In this fashion, data were gathered at all times between two camera triggers.

Fig. S5 shows a three-color confocal and ISM image of a cell with labeled actin (Alexa 488, blue), tubulin (Alexa 568, green), and paxillin (Alexa 647, red). The sample is the same as that described in the main text. Each image of the ISM raw data were averaged over 35 or 95 laser pulse sequences for 488 nm or 561/647 nm excitation, respectively, to achieve a good signal-to-noise ratio.

Fast 3D Imaging of Tau Protein

Movie S1 shows 3D projections of CSD data (*Upper*) and CSD-ISM data (*Lower*) of Tau protein aggregates, both processed with 3D deconvolution.

Three-dimensional deconvolution of *z*-stack data were performed using Piotr Wendykier's ImageJ plugin: https://sites.google.com/site/piotrwendykier/software/deconvolution/paralleliterativedeconvolution.

For deconvolution, we used the ISM data before Fourier reweighting and a theoretical ISM PSF, obtained by stretching the Fourier components of the 2D wide-field PSF by a factor of two, as described in *Fourier Reweighting*. The 3D PSF is composed of 31 2D PSFs for different focus positions separated by 100 nm. The settings for the deconvolution were Wiener Filter Preconditioned Landweber (WPL), Reflexive, Auto, Same as source, Double, and Max 10–50 iterations. The WPL options were Normalize PSF, Perform anti-ringing step, Detect divergence, Gamma 0, Low pass 1, and Termination 0.01.

Four-Color 3D Imaging

Fig. S4 shows a confocal image of a cell and the CSD-ISM image after 3D deconvolution of the same cell. Details on the sample preparation may be found in the main text. A movie of 3D projections of this cell is available as Movie S2.

Measurement of Nuclear Pore Complex Density

Nuclear pore density was measured with the ITCN ImageJ plugin, as described in *Methods*. An example of the performance of the ImageJ plugin with conventional spin disk and with ISM data is shown in Fig. S6. The region of interest in which nuclear pore complexes (NPCs) are detected is shown as a yellow oval in the upper panel. The NPCs found by the plugin are marked in red in the lower panel. Manually added NPC locations are marked in black.

1. Müller CB, Enderlein J (2010) Image scanning microscopy. *Phys Rev Lett* 104(19):198101.
2. Wolter S, et al. (2010) Real-time computation of subdiffraction-resolution fluorescence images. *J Microsc* 237(1):12–22.
3. Somekh MG, Hsu K, Pitter MC (2008) Resolution in structured illumination microscopy: A probabilistic approach. *J Opt Soc Am A Opt Image Sci Vis* 25(6):1319–1329.
4. Hsu K, Somekh MG, Pitter MC (2009) Stochastic transfer function: Application to fluorescence microscopy. *J Opt Soc Am A Opt Image Sci Vis* 26(7):1622–1629.
5. Somekh MG, Hsu K, Pitter MC (2009) Stochastic transfer function for structured illumination microscopy. *J Opt Soc Am A Opt Image Sci Vis* 26(7):1630–1637.

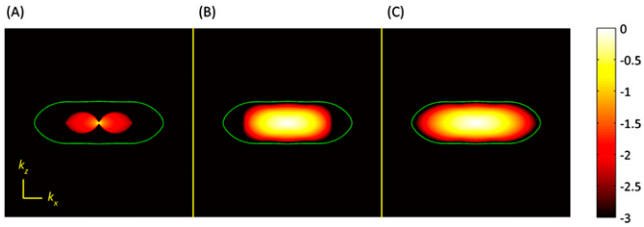

Fig. S1. Comparison of the OTFs of a wide-field microscope (*A*), a confocal microscope (*B*), and an ISM (*C*). The solid line delimits the region of maximally possible support of an optical diffraction-limited microscope. The direction of k_z is along the optical axis; the direction of k_x is perpendicular to the optical axis. The color scale gives the decadic logarithm of the normalized OTFs. The full 3D OTFs are obtained by rotating the figures shown around the optical axis.

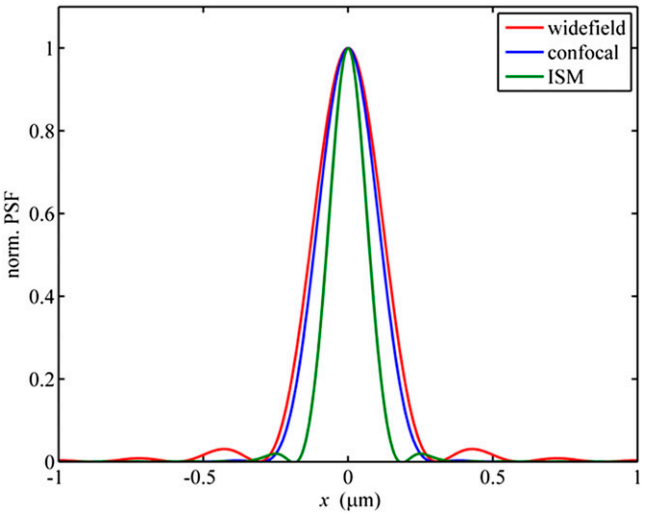

Fig. S2. Comparison of the lateral cross-sections of the PSF of a wide-field microscope, a confocal microscope, and an ISM microscope. The PSF of ISM is calculated after Fourier reweighting of its OTF, as described in the text.

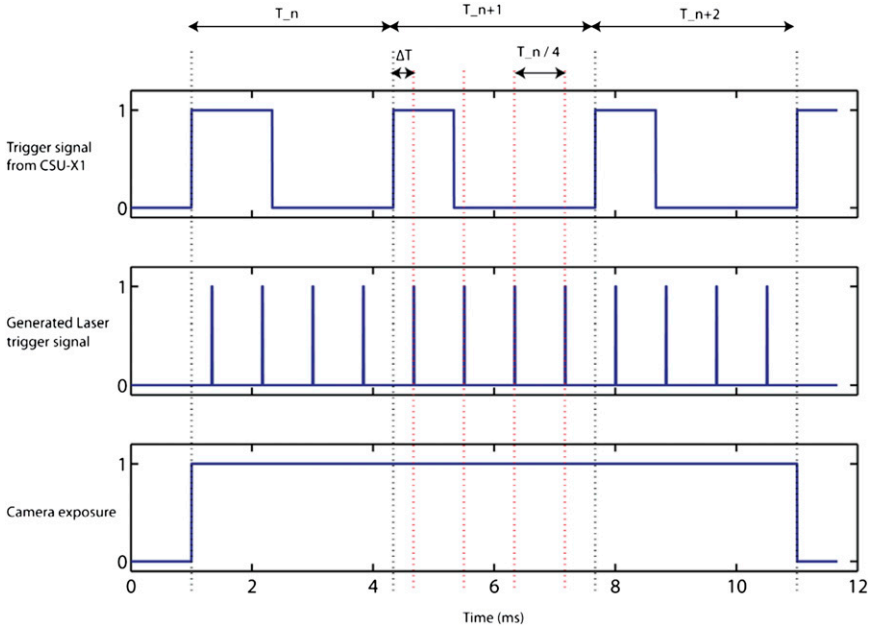

Fig. S3. Generation of trigger signals for CSD-ISM. See *Synchronization and Data Acquisition* for details.

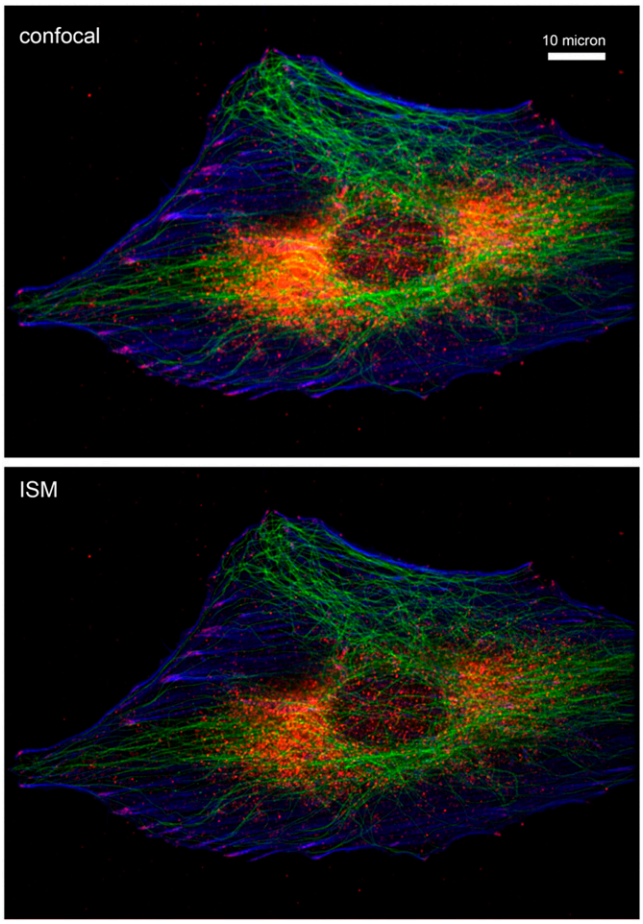

Fig. S4. sCMOS CSD-ISM images of a multicolor labeled HeLa cell. See *CSD-ISM with an sCMOS Camera* for details.

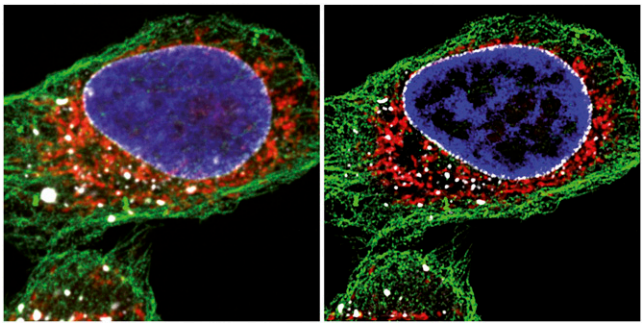

Fig. S5. HeLa P4 cell, as described in the main text. The cells were stained with Hoechst 33258 (blue) and MitoTracker M-7510 (red). α-Tubulin (green) and Nup358 (white) were detected by using specific antibodies and were visualized using Alexa 488- and Alexa 633-coupled secondary antibodies, respectively. (*Left*) CSD image; (*Right*) CSD-ISM image after 3D deconvolution using a theoretical ISM PSF. The image size is 33 μm.

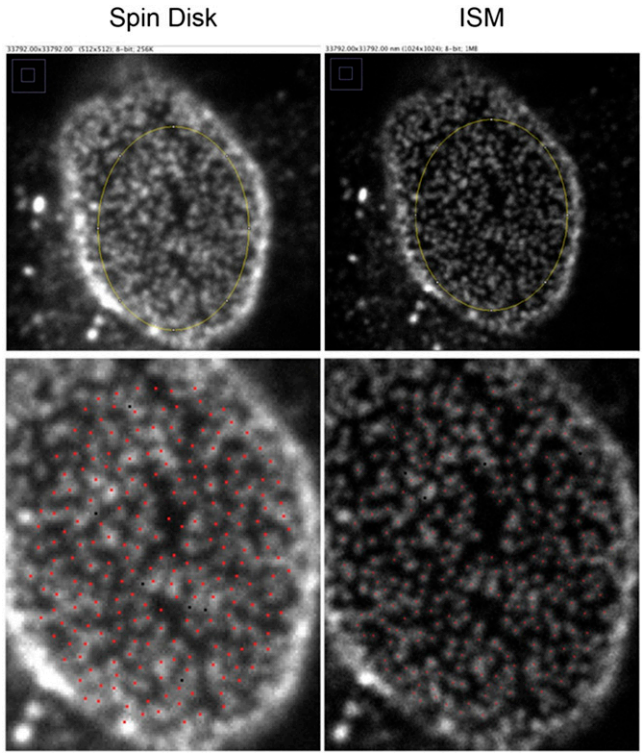

Fig. S6. Automated counting of NPCs on the nuclear membrane. (*Upper*) Region of interest used for the counting plugin. (*Bottom*) Red dots are found by the ImageJ plugin; black dots were added manually.

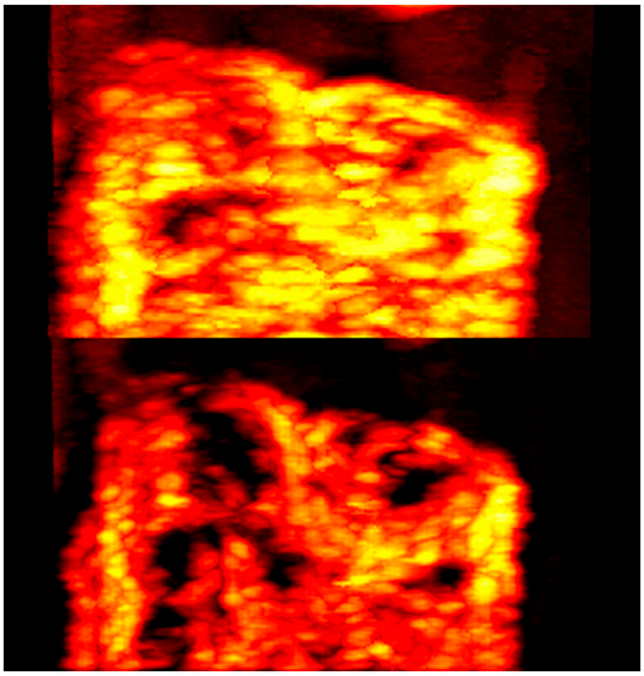

Movie S1. Three-dimensional projections of CSD data (*Upper*) and CSD-ISM data (*Lower*) of Tau protein aggregates, both processed with 3D deconvolution. Each of the 85 CSD-ISM images in the stack was acquired within 1 s. The distance between slices is 200 nm. For details, see Fast 3D Imaging of Tau Protein in the main text.

Movie S1

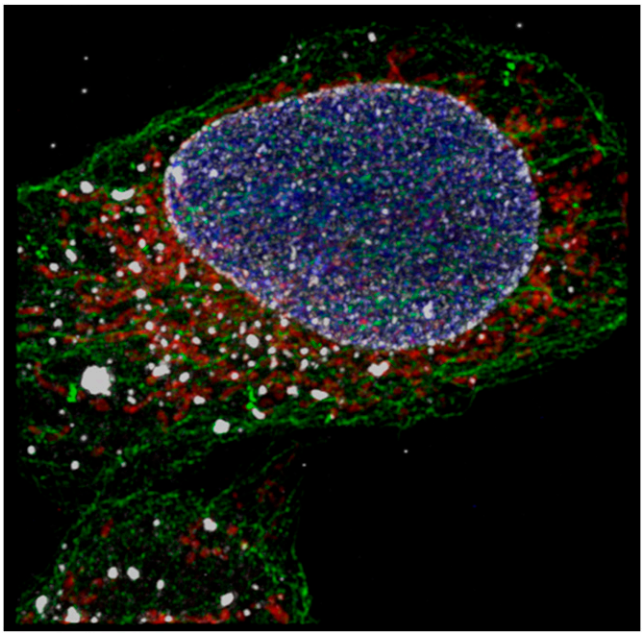

Movie S2. Three-dimensional projections of a four-color labeled cell as described in the main text. The distance between slices is 100 nm. The data were processed using 3D deconvolution.

Movie S2